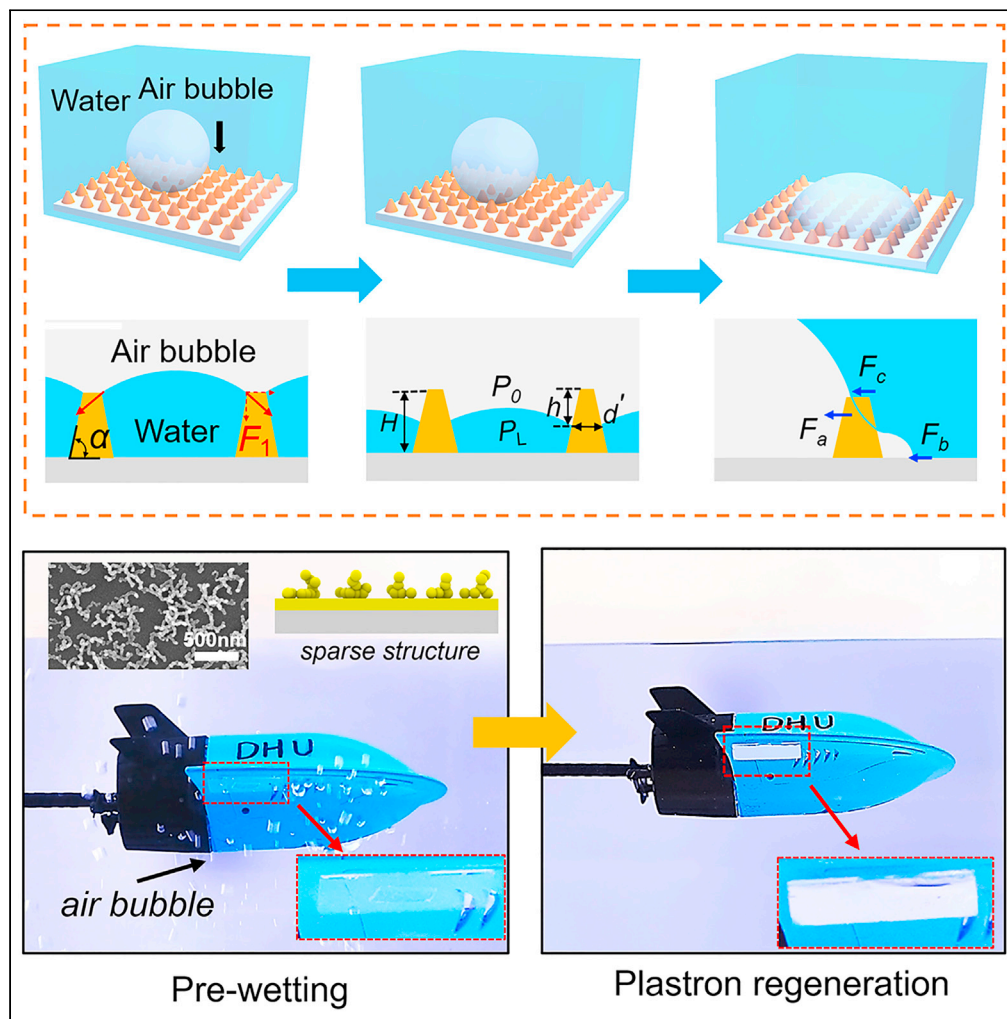


Article

# Recoverable underwater superhydrophobicity from a fully wetted state via dynamic air spreading



Yiping Zhao, Zhao Xu, Lu Gong, ..., Chunju He, Dengteng Ge, Lili Yang

liliyang@dhu.edu.cn

Highlights

Superhydrophobicity is recovered from fully wetted state in submerged system

The dynamic spreading of bubbles is theoretically analyzed

The geometric criteria provide direction in designing superhydrophobic surfaces



## Article

## Recoverable underwater superhydrophobicity from a fully wetted state via dynamic air spreading

Yiping Zhao,<sup>1,2</sup> Zhao Xu,<sup>1,2</sup> Lu Gong,<sup>3</sup> Shu Yang,<sup>4</sup> Hongbo Zeng,<sup>3</sup> Chunju He,<sup>1</sup> Dengteng Ge,<sup>2</sup> and Lili Yang<sup>1,5,\*</sup>

## SUMMARY

**Maintaining the superhydrophobicity underwater offers drag resistance reduction, antifouling, anti-corrosion, noise reduction, and gas collection for boat hulls and submarine vehicles. However, superhydrophobicity typically does not last long underwater since the Cassie state is metastable. Here, we report a reversible and localized recovery of superhydrophobicity from the fully wetted state via air bubble spreading. Composed of sparse fluorinated chained nanoparticles, the submerged surface shows super-low energy barrier for bubble attachment. Especially the recovered plastron exhibits excellent longevity. Based on a simplified, truncated nanocone model, the dynamic spreading of bubbles is analyzed considering two basic parameters, i.e., surface geometric structure and surface energy (which appeared as intrinsic water contact angle). Numerical simulation results via COMSOL confirms the effect of geometric structure on bubble spreading. This investigation will not only offer new insights for the design of robust recoverable superhydrophobic surfaces but also broaden the applications of superhydrophobic coatings.**

## INTRODUCTION

Surfaces that can maintain superhydrophobicity underwater are of great interest for ship hulls and submarine vehicles for potential applications including underwater breath (Flynn and Bush, 2008), gas collection (Yong et al., 2018), drag reduction (Srinivasan et al., 2015; Wang et al., 2014), antifouling (Wang et al., 2019), anti-corrosion (Vilaró et al., 2017; Zhang et al., 2020), and acoustic blocking (Huang et al., 2020). Bioinspired superhydrophobic surfaces (Feng et al., 2020; Gurumukhi et al., 2020; Li et al., 2019b) are usually achieved by hierarchical structures with low surface energy that keep a thin layer of air (plastron) trapped under water, named as the Cassie state (Cassie and Baxter, 1944). However, the plastron is metastable (Duan, 2017): large fluctuations of external conditions (such as pressure and liquid flow) can cause the superhydrophobic surface to transform from the Cassie state into the Wenzel state or fully wetted state. Much effort has been devoted to extending the entrapment time of plastron via micro-nano structure design (Domingues et al., 2018; Hu et al., 2017; Liu and Kim, 2014). Nevertheless, this passive strategy is not able to eliminate the hidden risk of submarine vehicles during practical applications once plastron is disrupted. Therefore, the active replenishment of plastron from the wetted state will be highly desired, e.g., (1) using an external field, (2) *in situ* gas generation, and (3) gas injection. Despite the success of achieving temporary transition from the Wenzel state to the Cassie state using methods such as vibration (Boreyko and Chen, 2009), electrical (Manukyan et al., 2011), temperature (Adera et al., 2013), water pressure (Forsberg et al., 2011), or gas concentration (Ling et al., 2017; Vakarelski et al., 2013) changes, these approaches have not been tested in practical submerged environments. Plastron could be regenerated via *in situ* chemical reactions (Aebischer et al., 2013; Lee and Kim, 2011; Lee and Yong, 2015; Lloyd et al., 2017; Panchanathan et al., 2018); however, this strategy is not repeatable or localizable. In contrast, the gas injection method (de Maleprade et al., 2016; Ma et al., 2015), viz. using injected gas bubbles on the aerophilic surfaces to recover plastron by draining liquid film, is simple, reversible, localizable, and instantaneous. Dewetting transition between the Cassie and partial Wenzel states on hierarchically structured surface has been observed (Boreyko and Collier, 2013; Verho et al., 2012; Wu et al., 2017) owing to the retention of nano-plastron. The effects of geometric parameters on the dewetting on cone/pillar arrays have been theoretically discussed (Li et al., 2019a; Zhang et al., 2016). However, two key problems remain unresolved: (1) no report is available on reversible recoverable superhydrophobicity from the fully wetted state and (2) no general geometric criteria are provided for air bubble pinning and spreading to recover superhydrophobic surfaces.

<sup>1</sup>State Key Laboratory for Modification of Chemical Fibers and Polymer Materials, College of Materials Science and Engineering, Donghua University, Shanghai 201620, China

<sup>2</sup>Institute of Functional Materials, Donghua University, Shanghai 201620, China

<sup>3</sup>Department of Chemical and Materials Engineering, University of Alberta, Edmonton, Alberta T6G 1H9, Canada

<sup>4</sup>Department of Materials Science and Engineering, University of Pennsylvania, 3231 Walnut Street, Philadelphia, PA 19104, USA

<sup>5</sup>Lead contact

\*Correspondence:  
liliyang@dhu.edu.cn

<https://doi.org/10.1016/j.isci.2021.103427>



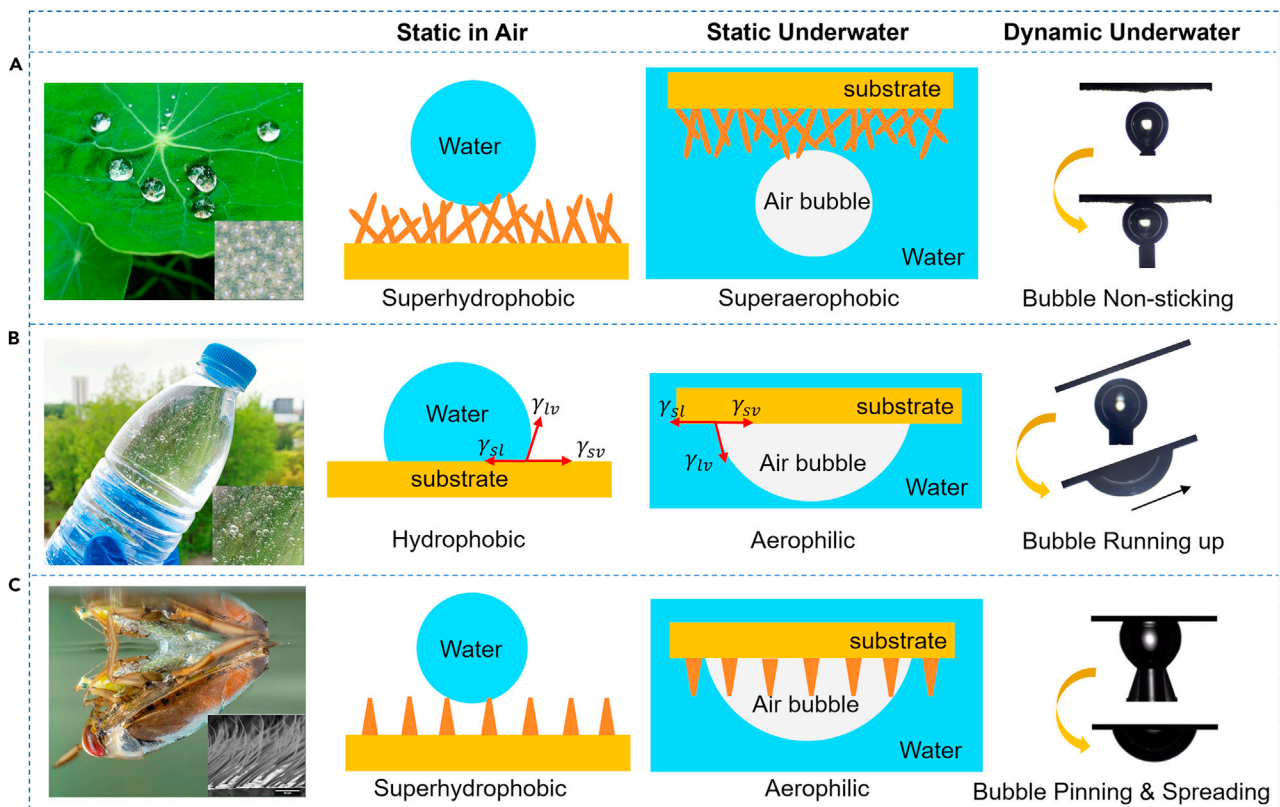


**Figure 1. Water/air behaviors on different surfaces**

(A) Optical image and SEM image of lotus leaf. Schematic for the lotus microstructures revealing superhydrophobicity in air but underwater superaerophobicity in the fully wetted state. Images from high-speed camera showing non-sticking bubble on wetted lotus leaf.  
 (B) A PET bottle of water with air bubbles. Schematic illustrations exhibiting the hydrophobicity in air and underwater aerophilicity of PET. Images from high-speed camera showing bubble running up on tilted PET sheet.  
 (C) A picture of water bug *Notonecta* and its SEM image of setae on the abdominal sternites. Schematic for a promising sparse microstructure with superhydrophobicity, aerophilicity that facilitate the pinning and spreading of air bubbles.

In order to achieve an underwater recoverable superhydrophobic surface from the fully wetted state via gas injecting, two questions should be addressed. First, is superhydrophobicity in air equivalent to underwater superaerophilicity? Various superhydrophobic surfaces have been proved to be superaerophobic in the fully wetted state but superaerophilic when plastron remains (Pei et al., 2018; Shan et al., 2018; Yong et al., 2019). As illustrated in Figure 1A, in air a water droplet cannot repel the gas anchored on the hierarchical structures. Vice versa, in an aqueous environment the air bubble cannot repel the water imbedded in the nanostructures. Video S1 shows a non-sticking bubble on the wetted lotus leaf. Second, is underwater aerophilicity sufficient to lead to the plastron recovery? As presented in Figure 1B, air bubble can adhere on the wall of the hydrophobic polyethylene terephthalate (PET) bottle, revealing underwater aerophilicity. However, the air bubble could not anchor and will disappear or run up under buoyancy (Video S1). Therefore, a nano/micro-structure that is both superhydrophobic and aerophilic to facilitate the pinning and spreading of air bubbles is required in order to recover the superhydrophobicity from the fully wetted state for submarine applications.

To design such a strategy, we have sought inspiration from the sparse hairy surface structure of nature aquatic arthropods of water bug (Ditsche-Kuru et al., 2011) or spider (Seymour and Hetz, 2011). As shown in Figure 1C, the water bug *Notonecta glauca* is surrounded by a thin film of air covering most of body parts with a silvery sheen appearance. Expectedly, a sparse nanostructure with low surface energy facilitates the bubble to repel the water in the nanostructure and regenerates plastron. In our previous work (Pei et al., 2018), an ultrathin superhydrophobic coating with two-tiered surface nanotextures assembled by chained nanoparticles shows excellent resistance to high water pressure or impingement of small water droplets.

Here we demonstrate, for the *first* time, a reversible, localized recovery of plastron from the fully wetted state using bubble injection. The unique sparse structure shows ultralow repulsive force of  $\sim 0.4$  nN to air bubbles with radius  $\sim 80$   $\mu\text{m}$  before the bubble-surface attachment under water. Furthermore, based on a simplified truncated nanocone model, dynamic bubble spreading behavior is studied considering two basic parameters, i.e., surface geometric structure and surface energy (appeared as intrinsic water contact angle). We develop basic criteria of nanotextured parameters for bubble adhesion and then lateral spreading without vertical growth. Modeling of the bubble spreading via COMSOL confirms the geometric effect of the surface structures.

## RESULTS

### Underwater air bubble behavior

As illustrated in [Figure S1](#) and our previous work ([Wu et al., 2021](#)), the fabrication of sparse microstructure for plastron recovery includes preparation of chained silica nanoparticles (NPs), dip-coating of chained NPs on a substrate functionalized by aminosilane, and fluorination treatment. The self-limiting deposition owing to the electrostatic repulsion and van der Waals force between the negatively charged silica NPs and easily percolated chain-like structures ensures a sparse fractal-like nanostructure ([Figure S2A](#)). The roughness and low surface energy endow the surface excellent superhydrophobicity ([Figure 2A](#)) with a water contact angle (WCA) of  $170 \pm 0.5^\circ$  and a rolling angle of  $1.0 \pm 0.5^\circ$  ([Table S1](#)) in air ([Figure S2B](#)). When the toy submarine coated with such superhydrophobic coating was immersed in water, a silver mirror-like reflectance could be visually observed, confirming the presence of plastron ([Figure 2A-i](#)). When it was dipped in ethanol to replace water, followed by resubmerging in water, a fully wetted state was achieved ([Figure S2](#) for details), as evident by the disappearance of the mirror-like interface ([Figure 2A-ii](#)). Gas bubbles could be injected using a needle but quickly moved onto the solid surface due to the buoyancy ([Figure 2A-iii](#)). Through the bubble pinning and spreading, the silvery sheen thus reappeared, indicating the plastron regeneration ([Figure 2A-iv](#), [Video S2](#)). Therefore, the superhydrophobicity could be recovered from the fully wetted state, which makes this surface function as a respiratory skin. Like the plastron replenishment of aquatic insects from gas dissolved in water, as illustrated in [Figure 2B](#), this surface on submarine vehicles endows the plastron recovery from the fully wetted state through simple external gas injection or submerged gas collection. This respiratory surface will enable submarine vehicles with drag reduction, anti-fouling, and anti-corrosion.

To validate the plastron recoverability as a result of the sparse nanostructure, we also evaluated fluorinated smooth glass substrate (denoted as Smooth in [Figure S2C](#)), multi-layered superhydrophobic surfaces (denoted as Multi-layered in [Figure S2E](#)). As listed in [Table S1](#), the WCAs on three surfaces in air are  $110^\circ$ ,  $165^\circ$ , and  $170^\circ$  and the rolling angles are  $90^\circ$ ,  $1.5^\circ$ , and  $1^\circ$ , respectively. Therefore, mirror-like interfaces are clearly visible and observed for the multi-layered and sparse nanostructured surfaces when directly immersed in water ([Figure 2C-i](#) and [Video S3](#)). In contrast, the smooth hydrophobic F-Glass was totally transparent because there was no gas trapped on the surface ([Video S3](#)). Then ethanol was dipped on all the three surfaces to wet them and achieve an underwater fully wetted state. When all three surfaces were re-immersed in water, none showed mirror-like sheen on the surface ([Figure 2C-ii](#)). When the surface was slowly pulled out and immersed in water again ([Figure 2C-iii](#)), silvery sheen reappeared only for the sparse surface ([Figure 2C-iv](#)).

For better understanding how air bubble interacts with surfaces of different textures, we monitored dynamic bubble contact angles (BCAs) on three submerged surfaces through releasing a small air bubble (50  $\mu\text{L}$ ) from the calibrated needle onto the pre-wetted surfaces ([Figure 2D](#) and [Video S4](#)). Once the gas bubble contacts the pre-wetted multi-layered surface with ethanol, a BCA of  $165^\circ$  was observed, suggesting superaerophobicity in water, and the bubble could be picked up easily with the needle. For the pre-wetted smooth F-glass, the bubble adheres to the smooth surface with a constant BCA of  $72^\circ$ , indicating the aerophilicity on the smooth hydrophobic surface but without lateral spreading. In contrast, when an air bubble contacts the wetted sparse surface, the bubble adheres to the surface and gradually spreads laterally, with the BCA decreased from  $122^\circ$  to  $75^\circ$  within 10 s.

In order to investigate the durability of recoverable superhydrophobic surface, three kinds of tests were carried out, i.e., the plastron monitoring with standing time, ethanol wetting-bubble injecting cycles, and different water pressure. As illustrated in [Figure 3A](#) and [Video S5](#), the recovered superhydrophobic surface via bubble injecting can retain its superhydrophobicity for more than 24 h. The silvery sheen is

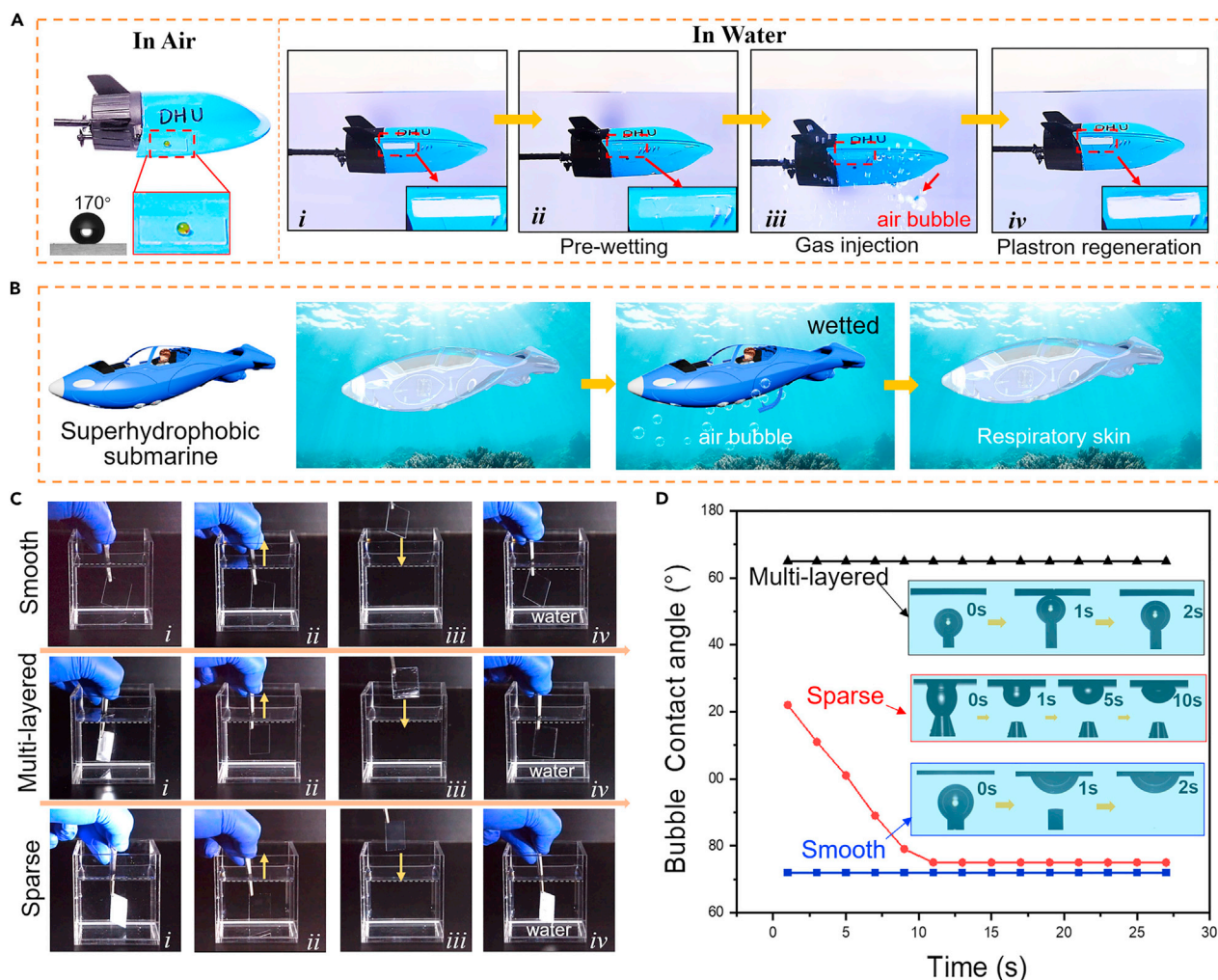


**Figure 2. Recoverable superhydrophobic surface from submerged fully wetted state**

(A) Optical images of our sparse surface on submarine toy showing the superhydrophobicity in air (i) submerged plastron appearing, (ii) pre-wetting, (iii) bubble injection, and (iv) plastron regeneration.

(B) Schematic illustrations for the applications in submarine vehicles as respiratory skin.

(C) Plastron evolution on three surfaces when samples are suspended underwater (i), after ethanol pre-wetting (ii), pulling out of water (iii), and re-entering into water (iv).

(D) Bubble contact angles monitoring of different submerged surfaces after ethanol pre-wetting.

maintained owing to the regenerated plastron from the stable visible reflectance (Figure S4). In addition, multiple ethanol wetting-bubble injecting cycles were also performed to further evaluate the recoverability of our superhydrophobic surface. Video S6 records the perfect plastron regeneration after many cycles. Figure 3B shows the water repellency of sample after the bubble injecting recovering. Even though the WCA and SA turn to  $158^\circ$  and  $10^\circ$  after 120 cycles, the plastron could be regenerated in our experiments. It is of great importance for the practical applications of recoverable superhydrophobic surfaces underwater. Last, the recovered superhydrophobic surface stability under various water pressures was also studied according to the laboratory-made test platform in Figure S5A. Our superhydrophobic surface was suspended 3 mm beneath the water. The water pressure is changed via gas injecting. From the reflectance monitoring (Figure S5B) and morphology observation of the superhydrophobic surface using optical microscopy (Video S7), it was found that the plastron becomes unstable when the water pressure is up to 25 kPa (Figure 3C). The solid-vapor interface was gradually replaced by the solid-liquid interface with the increase of water pressure. At a stronger water pressure of 40 kPa, the plastron disappeared, leading to a fully wetted state. Based on the maximum pressure comparison with reported surfaces (Figure S5C), this value

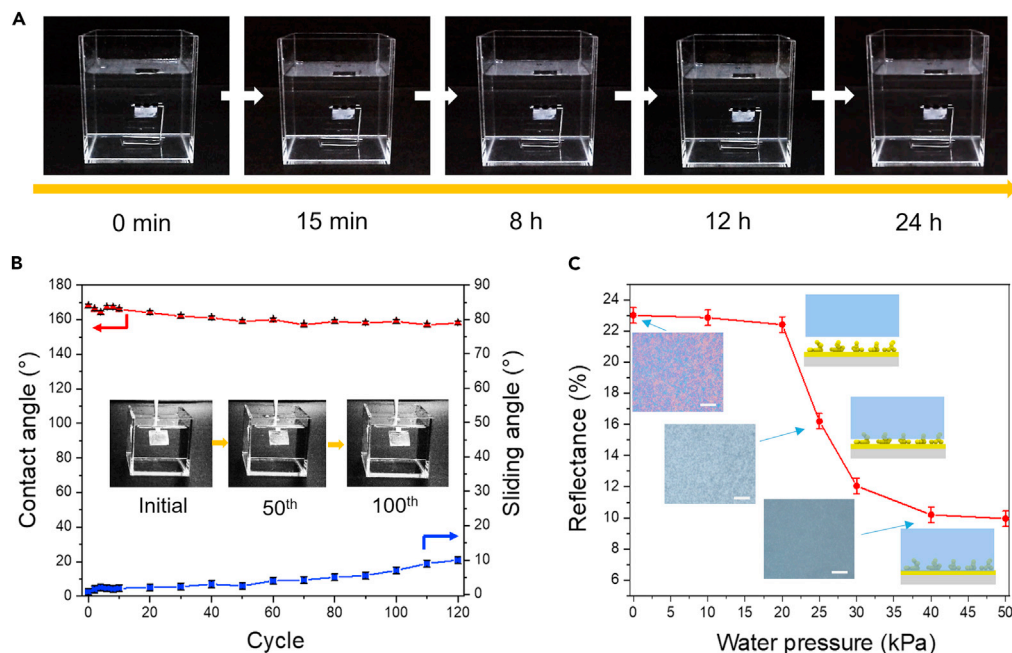


**Figure 3. Stability of recoverable superhydrophobic surfaces**

(A) Optical images of recovered plastron after different standing time.

(B) Water repellency of superhydrophobic surfaces after various wetting-recovering cycles.

(C) Reflectance at 550 nm of recovered superhydrophobic surface at different water pressures. Scale bar: 20  $\mu$ m.

in our work is much higher than that of lotus leaf (13.5 kPa), a hierarchical structure, but lower than that of SH surface with cylindrical micropores.

### Interaction force measurements

The interaction forces between air bubbles and submerged solid surfaces across the thin water film are directly measured using an atomic force microscope (AFM) bubble probe technique as shown in [Figure 4A](#) ([Shi et al., 2015b](#); [Xie et al., 2017](#)). When the surface is directly placed underwater (denoted as non-wetted state), the plastron between the submerged superhydrophobic surface and water allows the air bubbles to merge together rapidly. This phenomenon is consistent with the measured ultralow repulsive force, 0.3 nN for the sparse nanostructured surface ([Figure 4B](#)) or 0.05 nN for the multi-layered surface ([Figure S6A](#)) with an air bubble of radius  $\sim 80$   $\mu$ m before bubble-surface attachment. The force is a combination of the electrical double layer repulsion, van der Waals forces, hydrophobic attraction, and hydrodynamic repulsion for the bubble-water-surface system. The weaker repulsive force measured for the non-wetted multi-layered surface is probably because more gas is trapped in the multilayered porous surface, which may lead to the stronger hydrophobic attraction. In contrast, a very strong repulsive force ( $\sim 100$  nN) is measured for the non-wetted smooth F-glass due to the absence of the hydrophilic gas layer ([Figure S6B](#)). Once the surfaces are pre-wetted using ethanol in air, the surfaces are fully wetted when placed underwater, denoted as pre-wetted state. When sparse surface is pre-wetted, the air bubble can be easily “divorced” from the cantilever by overcoming a small repulsive force barrier of  $\sim 0.4$  nN ([Figure 4C](#)). The depletion of the thick continuous air layer on the sparse surface due to the pre-wetting by ethanol resulted in the weakened hydrophobic attraction between the air bubble and the surface. Hence, a little stronger pressing force was needed for the bubble to repel water in sparse nanostructure. As shown in [Figure 4D](#), the air bubble can be forced to attach to the pre-wetted F-Glass surface after overcoming a stronger repulsive force of  $\sim 105$  nN, which is close to the repulsive force barrier for the non-wetted case, suggesting the negligible influence of the pre-wetting process due to the absence of gas layer on the smooth F-glass. The bubble cannot be picked up by the cantilever during separation ([Figure 4D](#)), consistent with the bubble contact angle tests in [Figure 2D](#). In contrast, the air bubble cannot spread on the pre-wetted multi-layered surface but can be directly picked up by the cantilever with a strong adhesion of  $\sim 200$  nN ([Figure 4E](#)). The

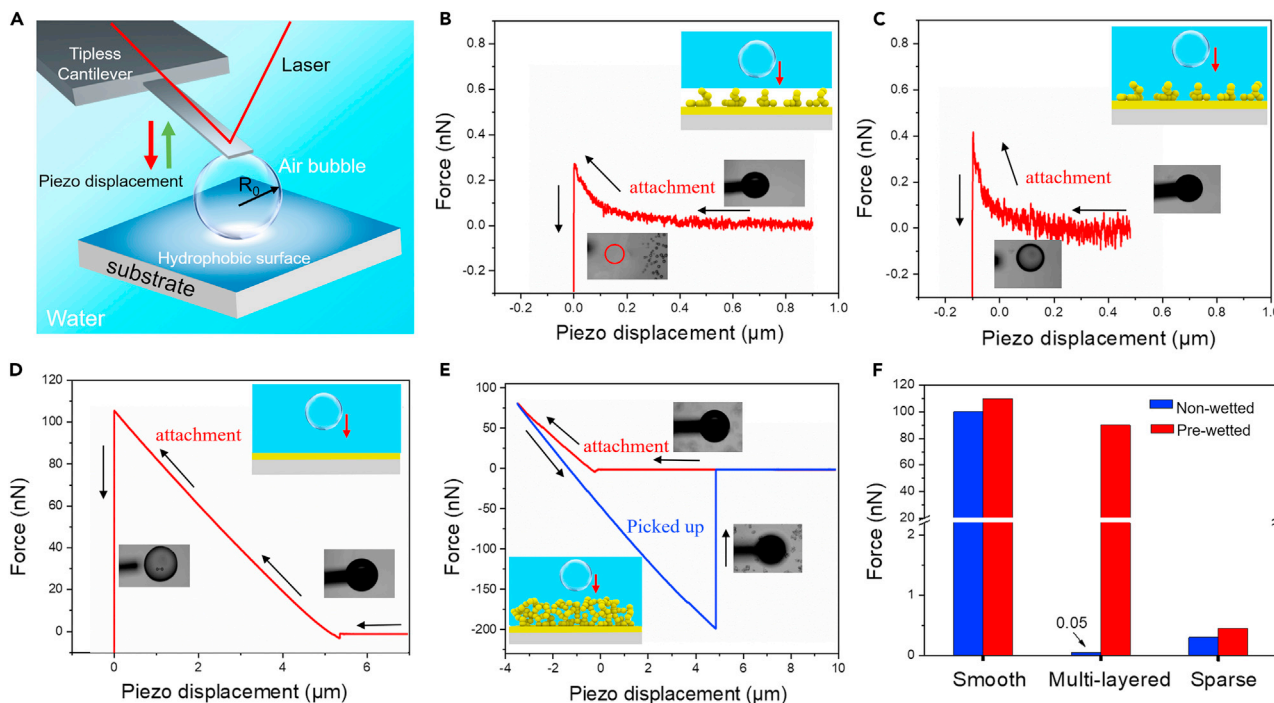


**Figure 4. Interaction force measurements between an air bubble and submerged solid surfaces**

(A) Schematic for the interaction force measurements using the AFM bubble probe technique. (B–E) Measured force profiles between air bubbles of radius  $\sim 80 \mu\text{m}$  of (B) submerged non-wetted sparse surface, (C) submerged pre-wetted sparse surface, (D) submerged pre-wetted smooth surface, and (E) submerged pre-wetted multi-layered surface. (F) Maximum repulsion measured between air bubbles and different hydrophobic surfaces.

detachment behavior of the bubble from the multi-layered surface indicates that the bubble cannot repel water trapped in the nanostructure. These results were consistent with what we observed in air bubble contact angle measurement (Figure 4F).

### Theoretical dynamic analysis

In order to develop general geometric criteria for the nanostructure design that can enable plastron recovery via air injecting, we built a simplified truncated cone model for calculation. As illustrated in Figure 5A,  $\alpha$ ,  $d$ ,  $D$ ,  $H$ , and  $L$  represent the bottom angle, top diameter, bottom diameter, height, and pitch (center-to-center distance), respectively. The dewetting transition from the fully wetted state to the Cassie state involves three basic stages: (1) air bubble adhering to the top surface of nanostructure (Figure 5A-i); (2) downward repelling of water, pushing water out, and completely filling the nanostructure in the local contact region (Figure 5A-ii); (3) pushing water out of the neighboring nanostructures laterally and spreading the air bubble without vertical outgrowth (Figure 5A-iii). Here our sparse structure could be simplified as  $H = 120 \text{ nm}$ ,  $L = 1,000 \text{ nm}$ ,  $D = 350 \text{ nm}$ ,  $d = 150 \text{ nm}$ , and  $\alpha = 60^\circ$  (Figure S7).

Once the air bubble contacts the top surface of the nanostructure, it will adhere to the top if the interfacial tension at the air/solid/water contact line points to the bottom. The resultant vertical force due to surface tension,  $F_1$ , can be described as (details in supplemental information):

$$F_1 = \gamma \pi d' \sin(\theta - \alpha) \quad (\text{Equation 1})$$

where  $\gamma$  and  $d'$  represent the surface tension of water and the corresponding section diameter when bubble contacts with truncated cone, respectively. Here  $\theta$  stands for the intrinsic water contact angle, equivalent to the WCA on a smooth surface (e.g., F-Glass). Thus  $\theta = 110^\circ$ . Assuming  $d' = d = 150 \text{ nm}$ , it is deduced that the air bubble could adhere to the top surface when  $\alpha \leq 110^\circ$ , but would be picked up with the gas injection string when  $\alpha > 110^\circ$  (Figure 5B).

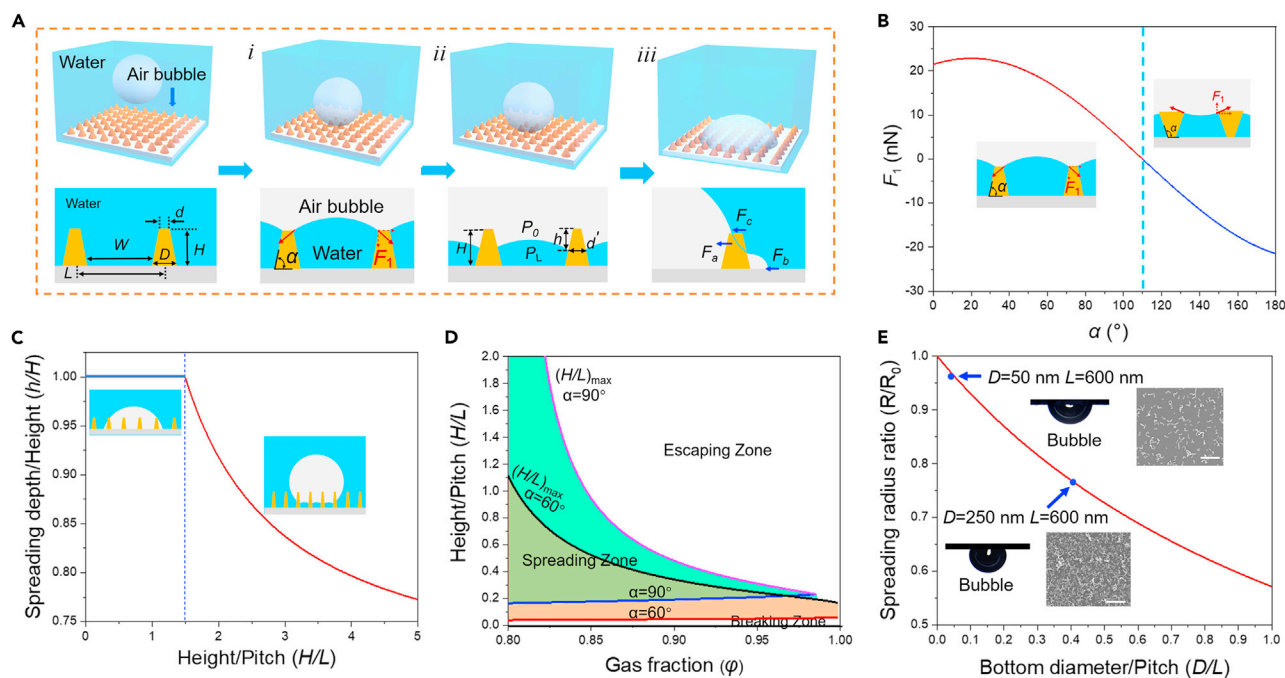


**Figure 5. Schematic and results of theoretical analysis**

- (A) Schematic of bubble dynamic spreading process for plastron regeneration.  
 (B) The relationship between bottom angle  $\alpha$  and the surface tension of air-water interface.  
 (C) The relationship between height/pitch ( $H/L$ ) and spreading depth/height ( $h/H$ ).  
 (D) Estimated range of height/pitch ratio ( $H/L$ ) and gas fraction ( $\varphi$ ) for bubble escaping, spreading, or breaking.  
 (E) The relationship between bottom diameter/pitch ( $D/L$ ) and spreading radius ratio ( $R/R_0$ ). Scale bar: 1  $\mu\text{m}$ .

Once adhering to the top surface, the air bubble is also required to gradually repel the water in the neighboring nanostructures and finally fill the whole cavity. Based on Boyle's law of air bubble during the dynamic vertical spreading in the cavity, there is relationship as follows (details in [supplemental information](#)):

$$\frac{h}{H} = \frac{P_0}{P_L + \frac{8\pi(D+d)\cos\theta}{16L^2 - \pi(D+d)^2}\gamma} - \frac{[2\sqrt{2} - (d+D)/L]}{12\cos^3\theta} \frac{1}{H/L} (2 - 3\sin\theta + \sin^3\theta) \quad (\text{Equation 2})$$

where  $P_0$  and  $P_L$  represent the air bubble pressure and water pressure, respectively. In order to study the filling depth of air bubble into the nanostructure, here we assume  $P_0 = 101.3$  kPa,  $P_L = 150$  kPa (depth of 15 cm water),  $d = 50$  nm,  $D = 250$  nm,  $L = 600$  nm,  $\theta = 110^\circ$ . As illustrated in [Figure 5C](#), for the nanostructures with a specific sparsity (determined by  $D/L$ ), as the height to pitch of the nanostructure ( $H/L$ ) is  $> 1.5$ , the air bubble would not reach the bottom (the inset image in [Figure 5C](#)). Thus the plastron cannot be regenerated from that fully wetted state.

In the third stage, the air bubble is expected to continue lateral spreading without vertical outgrowth. Laterally, the air bubble overcomes the viscous force on air/solid interfaces to repel the water in the neighboring nanostructure ([Figure S12](#)). Vertically, the internal pressure of the air bubbles should not be too large for them to escape from the interface or too small to break. By modifying the calculations for the post model, we give the criteria for the truncated cone model as follows (details in [STAR Methods](#)):

$$\left(\sqrt{2} - 2\sqrt{(1-\varphi)/\pi}\right) \frac{1 - \sin(270^\circ - \alpha - \theta_{adv})}{2\cos(270^\circ - \alpha - \theta_{adv})} < H/L < \frac{-\cos\theta\sin\alpha}{2\sin\theta(1 - \sin\alpha\sqrt{\pi(1-\varphi)})/\varphi} \quad (\text{Equation 3})$$

where  $\varphi$  represents the gas fraction in Cassie state and here  $\varphi = 1 - \frac{\pi d^2}{4L^2}$  for truncated nanocone model.  $\theta_{adv}$  is the advancing contact angle on the truncated nanocone surface, which is  $130^\circ$  based on our experimental results ([Figure S14](#)). According to the Cassie-Baxter equation, the apparent water contact angle  $\theta_c$ ,

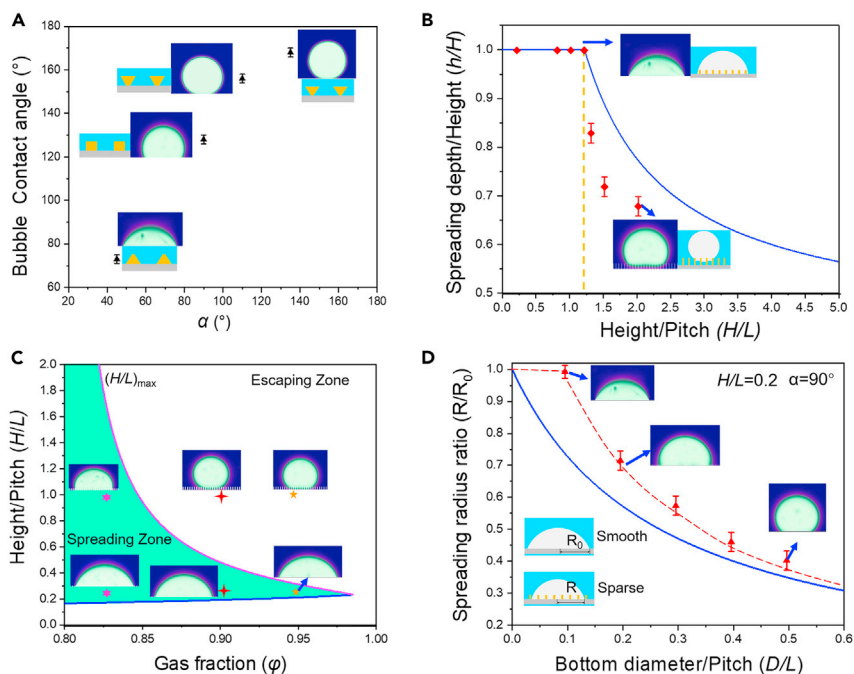


**Figure 6. Simulation results of air bubble dynamic spreading on surfaces with different geometric parameters**

(A) Bubble contact angles with different bottom angles.

(B) Theoretical spreading depth/height ( $h/H$ ) (blue line) and simulated results (red line) with different height/pitch ( $H/L$ ).

(C) Bubble contact angles with different gas fraction and height/pitch ( $H/L$ ).

(D) Spreading diameter ratio with different bottom diameter/pitch ( $D/L$ ).

$$\cos \theta_c = (1 - \phi) \cos \theta - \phi \quad (\text{Equation 4})$$

Thus,  $\phi$  should be greater than 0.8 to achieve superhydrophobicity ( $\theta_c > 150^\circ$ ) in air based on  $\theta = 110^\circ$ . Figure 5D shows three zones (breaking zone, spreading zone, and escaping zone) based on the geometric boundaries of  $H/L$   $\phi = 0.8 \sim 1$ . With the increase of  $\phi$ , the window of  $H/L$  for lateral spreading of the air bubble is too narrow. Therefore, nanostructures with modest sparsity are in favor of air bubble spreading without escaping from the surface. Moreover, when  $\alpha$  increases from  $60^\circ$  to  $90^\circ$ , the spreading zone is widened. Moreover, if we could increase the Young's water contact angle on a smooth surface  $\theta$  from  $110^\circ$  to  $130^\circ$ , the boundary of  $H/L$  would be much wider (Figure S15). Thus moderate sparsity and further reduction of surface free energy are two effective strategies to achieve stable air bubble spreading on nanostructures.

Last, the spreading radius of the air bubble  $R$  on the truncated nanocone surface is predicted by considering the lateral viscous forces resulting from the movement of air/solid/water contact line only. Supposing the initial spreading radius on F-Glass is  $R_0$ ,

$$\frac{R}{R_0} = \frac{-\cos \theta}{\frac{D}{L} \frac{\sin \theta}{5} - \cos \theta - \frac{D}{L} \frac{\cos \theta}{5}} \quad (\text{Equation 5})$$

If  $\theta = 110^\circ$  and  $d = D/5$ , Figure 4E shows that smaller  $D/L$  (i.e., higher sparsity) facilitates the spreading of air bubbles and thus plastron recovery. Thus, sparse superhydrophobic surfaces with different sparsity were prepared through the control of dipping time in chained NPs solution. Scanning electron microscopy (SEM) images and bubble wetting tests suggested that the experimental results (blue dots in Figure 5E) were consistent with the theoretical prediction (red line).

### Numerical simulations

In order to verify the theoretical prediction, the bubble dynamic spreading on the submerged surface was numerically studied based on two-phase flow and level set method via COMSOL software. By adjusting

different geometric parameters, the bubble contact angle and three-phase contact line were monitored. [Figure 6A](#) and [Video S8](#) show the bubble contact angles on the nanostructured surfaces with different  $\alpha$  but the same  $D/L$  or  $H/L$ . At  $\alpha \geq 110^\circ$ , the bubble contact angle is greater than  $150^\circ$ , causing the bubble to easily escape the surface under buoyancy. [Figure 6B](#) presents the bubble spreading depth/height ( $h/H$ ) with varying height/pitch ( $H/L$ ) of the post structured surface from theoretical results (blue line) and simulated results (red dots). According to [Equation 2](#), bubbles would not reach the posts' bottom when  $H/L > 1.25$ . The simulation indicates that the bubble could reach the bottom of posts when  $H/L = 1.2$  but not when  $H/L = 1.3$ , which is exactly consistent with the theoretical results. [Figure 6C](#) demonstrates the bubble wetting behavior on post structured surface with varying  $\phi$  and  $H/L$ . When  $D/L = 0.25, 0.36, \text{ or } 0.47$ ,  $\phi = 0.95, 0.90, \text{ or } 0.83$ , respectively. For a surface with high gas fraction ( $\phi = 0.95$ ), the bubble would be unstable vertically when  $H/L = 1$  ( $\text{BCA} = 135^\circ$ ). In contrast, the bubble is stable vertically until  $H/L = 1$  for surface with low gas fraction ( $\phi = 0.83$ ). Finally, the spreading radius ratio of bubble on post with different  $D/L$  was also summarized from the simulated results ([Figure 6D](#)). Similar to the theoretical results, the spreading radius of bubble decreases with the increase of diameter/pitch ( $D/L$ ). The spreading radius of bubble from theoretical results is lower than that from simulated ones, mainly because we used the maximum viscous forces during calculation. According to the comparison, it is believed that our geometric criteria given from theoretical calculation are highly effective for the designing of recoverable superhydrophobic surfaces.

## Conclusions

The metastable Cassie state in submerged underwater environments could severely destroy the superhydrophobic surfaces. Many aquatic insects and spiders with sparse, hairy surfaces can survive when submerged by virtue of plastron replenishment from gas dissolved in water. Mimicking Nature, we create aerophilic surfaces as a respiratory skin for submarine vehicles, which facilitates the air bubble pinning and stable spreading on the skin, allowing for underwater recovery of the superhydrophobic surface from the fully wetted state using bubble injection. Through the self-limited assembly of chained NPs on the surface, a super-low repulsive force barrier (0.4 nN) is measured for bubble attachments upon being submerged in water. The durability tests demonstrate that the recovered plastron can suffer from standing for more than 24 h, 120 cycles of ethanol wetting-bubble injection, and high water pressure (<25 kPa). Considering two basic parameters, i.e., surface geometric structure and surface energy (which appeared as the intrinsic water contact angle), the dynamic process of bubbles on a simplified truncated nanoconed surface was analyzed. We further obtained specific geometric criteria for the air bubble pinning and lateral spreading without vertical escaping, which are validated by the numerical simulation. The study here offers new insights for the design of recoverable underwater superhydrophobic surfaces, where the air bubble pinning and stable spreading on such surfaces are essential. In turn, it will broaden the applications of superhydrophobic coatings to underwater environments, where, for example, drag reduction, anti-fouling, anti-corrosion, and underwater breath are important for the operation and lifetime of ship hull, submarine vehicles, and equipment but have remained challenging to achieve so far because of the metastable nature of the nonwetting Cassie state.

## Limitation of the study

There are many parameters that influence the attachment behaviors of air bubbles on the surfaces underwater, including surface roughness, surface chemical modification, temperature, electric double layer, pH, and water pressure. However, it is difficult to consider each parameter independently in theoretical analysis and numerical simulation. Here, the effect of pH or electric double layer or temperature is involved in the basic parameter, i.e., the intrinsic water contact angle  $\theta$ . The effect of water pressure is out of consideration owing to the great complexity for theoretical analysis and numerical simulation.

## SUPPORTING CITATIONS

[Lv et al., 2014](#); [Sheng and Zhang, 2011](#); [Zeiger et al., 2017](#).

## STAR★METHODS

Detailed methods are provided in the online version of this paper and include the following:

- KEY RESOURCES TABLE
- RESOURCE AVAILABILITY
- Lead contact

- Materials availability
- Date and code availability
- **EXPERIMENTAL MODEL AND SUBJECT DETAILS**
- **METHODS DETAILS**
  - Preparation of recoverable superhydrophobic surfaces
  - Fabrication of F-Glass and multi-layered superhydrophobic surfaces
  - Characterization
  - Interaction forces between air bubbles and surfaces
  - Calculations for the simplifying the sparse surface from chained NPs into truncated nanocone model
  - Calculations for the geometric criteria of truncated nanocone model that allows the air bubble adhere to the top
  - Calculations for the geometric criteria of truncated nanocone model that allows the air bubble fill the closest microstructure
  - Calculations for the geometric criteria of truncated nanocone model that allows the air bubble continue lateral spreading without vertical outgrowth
  - Calculations of spreading radius of air bubble on truncated nanocone microstructured surface
  - Dynamic simulation
- **QUANTIFICATION AND STATISTICAL ANALYSIS**

## SUPPLEMENTAL INFORMATION

Supplemental information can be found online at <https://doi.org/10.1016/j.isci.2021.103427>.

## ACKNOWLEDGMENTS

We thank the financial support from the National Natural Science Foundation of China 11604045 and 11774049 and the Fundamental Research Funds for the Central Universities 2232021D-02. H.Z. and L.G. acknowledge the support from the Natural Sciences and Engineering Research Council of Canada (NSERC), the Canada Foundation for Innovation (CFI), and the Canada Research Chairs Program.

## AUTHOR CONTRIBUTIONS

L.Y., D.G., S.Y., and H.Z. conceived the research idea and designed the experiments. Experiments and data analysis were performed by Y.Z., Z.X., S.Y., and D.G. Simulations were performed by Z.X. The manuscript was drafted by S.Y., H.Z., D.G., and L.Y. All authors have given their approval to the manuscript.

## DECLARATION OF INTERESTS

The authors declare no competing interests.

Received: August 31, 2021

Revised: October 6, 2021

Accepted: November 7, 2021

Published: December 17, 2021

## REFERENCES

- Adera, S., Raj, R., Enright, R., and Wang, E.N. (2013). Non-wetting droplets on hot superhydrophilic surfaces. *Nat. Commun.* *4*, 2518. <https://doi.org/10.1038/ncomms3518>.
- Aebischer, D., Bartusik, D., Liu, Y., Zhao, Y., Barahman, M., Xu, Q., Lyons, A.M., and Greer, A. (2013). Superhydrophobic photosensitizers. Mechanistic studies of  $^1\text{O}_2$  generation in the plastron and solid/liquid droplet interface. *J. Am. Chem. Soc.* *135*, 18990–18998. <https://doi.org/10.1021/ja410529q>.
- Boreyko, J.B., and Chen, C.-H. (2009). Restoring superhydrophobicity of lotus leaves with vibration-induced dewetting. *Phys. Rev. Lett.* *103*, 174502. <https://doi.org/10.1103/PhysRevLett.103.174502>.
- Boreyko, J.B., and Collier, C.P. (2013). Dewetting transitions on superhydrophobic surfaces: When are Wenzel drops reversible? *J. Phys. Chem. C* *117*, 18084–18090. <https://doi.org/10.1021/jp4053083>.
- Cassie, A.B.D., and Baxter, S. (1944). Wettability of porous surfaces. *Trans. Faraday Soc.* *40*, 546–551. <https://doi.org/10.1039/tf9444000546>.
- Cui, X., Liu, J., Xie, L., Huang, J., Liu, Q., Israelachvili, J.N., and Zeng, H.B. (2018). Modulation of hydrophobic interaction by mediating surface nanoscale structure and chemistry, not monotonically by hydrophobicity. *Angew. Chem. Int. Ed.* *57*, 11903–11908. <https://doi.org/10.1002/anie.201805137>.
- de Maleprade, H., Clanet, C., and Quere, D. (2016). Spreading of bubbles after contacting the lower side of an aerophilic slide immersed in water. *Phys. Rev. Lett.* *117*, 094501. <https://doi.org/10.1103/PhysRevLett.117.094501>.
- Ditsche-Kuru, P., Schneider, E.S., Melskotte, J.E., Brede, M., Leder, A., and Barthlott, W. (2011). Superhydrophobic surfaces of the water bug *Notonecta glauca*: A model for friction reduction

- and air retention. *Beilstein J. Nanotechnol.* 2, 137–144. <https://doi.org/10.3762/bjnano.2.17>.
- Domingues, E.M., Arunachalam, S., Nauruzbayeva, J., and Mishra, H. (2018). Biomimetic coating-free surfaces for long-term entrapment of air under wetting liquids. *Nat. Commun.* 9, 3606. <https://doi.org/10.1038/s41467-018-05895-x>.
- Duan, H.L. (2017). Underwater superhydrophobicity: Fundamentals and applications. *Procedia IUTAM* 20, 128–135. <https://doi.org/10.1016/j.piutam.2017.03.018>.
- Feng, L., Lo, S.H., Tan, K., Li, B.H., Yuan, S., Lin, Y.F., Lin, C.H., Wang, S.L., Lu, K.L., and Zhou, H.C. (2020). An encapsulation-rearrangement strategy to integrate superhydrophobicity into mesoporous metal-organic frameworks. *Matter* 2, 988–999. <https://doi.org/10.1016/j.matt.2020.01.015>.
- Flynn, M.R., and Bush, J.W.M. (2008). Underwater breathing: The mechanics of plastron respiration. *J. Fluid Mech.* 608, 275–296. <https://doi.org/10.1017/S0022112008002048>.
- Forsberg, P., Nikolajeff, F., and Karlsson, M. (2011). Cassie-Wenzel and Wenzel-Cassie transitions on immersed superhydrophobic surfaces under hydrostatic pressure. *Soft Matter* 7, 104–109. <https://doi.org/10.1039/c0sm00595a>.
- Ge, D.T., Yang, L.L., Zhang, Y.F., Rahmawan, Y., and Yang, S. (2014). Transparent and superamphiphobic surfaces from one-step spray coating of stringed silica nanoparticle/sol solutions. *Part. Syst. Charact.* 31, 763–770. <https://doi.org/10.1002/ppsc.201300382>.
- Gong, L., Xiang, L., Zhang, J.W., Han, L.B., Wang, J.Y., Wang, X.G., Liu, J.F., Yan, B., and Zeng, H.B. (2019). Interaction mechanisms of zwitterions with opposite dipoles in aqueous solutions. *Langmuir* 35, 2842–2853. <https://doi.org/10.1021/acs.langmuir.8b04091>.
- Gurumukhi, Y., Chavan, S., Sett, S., Boyina, K., Ramesh, S., Sokalski, P., Fortelka, K., Lira, M., Park, D., Chen, J.Y., et al. (2020). Dynamic defrosting on superhydrophobic and biphilic surfaces. *Matter* 3, 1178–1195. <https://doi.org/10.1016/j.matt.2020.06.029>.
- Hu, H.B., Wen, J., Bao, L.Y., Jia, L.B., Song, D., Song, B.W., Pan, G., Scaraggi, M., Dini, D., Xue, Q.J., et al. (2017). Significant and stable drag reduction with air rings confined by alternated superhydrophobic and hydrophilic strips. *Sci. Adv.* 3, e1603288. <https://doi.org/10.1126/sciadv.1603288>.
- Huang, Z., Zhao, S., Su, M., Yang, Q., Li, Z., Cai, Z., Zhao, H., Hu, X., Zhou, H., Li, F., et al. (2020). Bioinspired patterned bubbles for broad and low-frequency acoustic blocking. *ACS Appl. Mater. Interfaces* 12, 1757–1764. <https://doi.org/10.1021/acsami.9b15683>.
- Hutter, J.L., and Bechhoefer, J. (1993). Calibration of atomic-force microscope tips. *Rev. Sci. Instrum.* 64, 1868–1873. <https://doi.org/10.1063/1.1143970>.
- Lee, C., and Kim, C.J. (2011). Underwater restoration and retention of gases on superhydrophobic surfaces for drag reduction. *Phys. Rev. Lett.* 106, 014502. <https://doi.org/10.1103/PhysRevLett.106.014502>.
- Lee, J., and Yong, K. (2015). Combining the lotus leaf effect with artificial photosynthesis: Regeneration of underwater superhydrophobicity of hierarchical ZnO/Si surfaces by solar water splitting. *NPG Asia Mater.* 7, e201. <https://doi.org/10.1038/am.2015.74>.
- Li, X.J., Li, J.J., Peng, Z.L., and Chen, S.H. (2019a). Spontaneous dewetting of a hydrophobic micro-structured surface. *J. Phys. Condens. Matter* 31, 295001. <https://doi.org/10.1088/1361-648X/ab1998>.
- Li, Z., Cao, M.Y., Li, P., Zhao, Y.Y., Bai, H.Y., Wu, Y.C., and Jiang, L. (2019b). Surface-embedding of functional micro-/nanoparticles for achieving versatile superhydrophobic interfaces. *Matter* 1, 661–673. <https://doi.org/10.1016/j.matt.2019.03.009>.
- Ling, H.J., Katz, J., Fu, M., and Hultmark, M. (2017). Effect of Reynolds number and saturation level on gas diffusion in and out of a superhydrophobic surface. *Phys. Rev. Fluids* 2, 124005. <https://doi.org/10.1103/PhysRevFluids.2.124005>.
- Liu, T.Y., and Kim, C.J. (2014). Turning a surface superrepellent even to completely wetting liquids. *Science* 346, 1096–1100. <https://doi.org/10.1126/science.1254787>.
- Lloyd, B.P., Bartlett, P.N., and Wood, R.J.K. (2017). Active gas replenishment and sensing of the wetting state in a submerged superhydrophobic surface. *Soft Matter* 13, 1413–1419. <https://doi.org/10.1039/c6sm02820a>.
- Lv, P.Y., Xue, Y.H., Shi, Y.P., Lin, H., and Duan, H.L. (2014). Metastable states and wetting transition of submerged superhydrophobic structures. *Phys. Rev. Lett.* 112, 196101. <https://doi.org/10.1103/PhysRevLett.112.196101>.
- Ma, R., Wang, J.M., Yang, Z.J., Liu, M., Zhang, J.J., and Jiang, L. (2015). Bioinspired gas bubble spontaneous and directional transportation effects in an aqueous medium. *Adv. Mater.* 27, 2384–2389. <https://doi.org/10.1002/adma.201405087>.
- Manukyan, G., Oh, J.M., van den Ende, D., Lammertink, R.G.H., and Mugele, F. (2011). Electrical switching of wetting states on superhydrophobic surfaces: A route towards reversible Cassie-to-Wenzel transitions. *Phys. Rev. Lett.* 106, 014501. <https://doi.org/10.1103/PhysRevLett.106.014501>.
- Panchanathan, D., Rajappan, A., Varanasi, K.K., and McKinley, G.H. (2018). Plastron regeneration on submerged superhydrophobic surfaces using in situ gas generation by chemical reaction. *ACS Appl. Mater. Interfaces* 10, 33684–33692. <https://doi.org/10.1021/acsami.8b12471>.
- Pei, C.T., Peng, Y., Zhang, Y., Tian, D.L., Liu, K.S., and Jiang, L. (2018). An integrated janus mesh: Underwater bubble antibuoyancy unidirectional penetration. *ACS Nano* 12, 5489–5494. <https://doi.org/10.1021/acsnano.8b01001>.
- Seymour, R.S., and Hetz, S.K. (2011). The diving bell and the spider: The physical gill of *Argyroneta aquatica*. *J. Exp. Biol.* 214, 2175–2181. <https://doi.org/10.1242/jeb.056093>.
- Shan, C., Yong, J.L., Yang, Q., Chen, F., Huo, J.L., Zhuang, J., Jiang, Z.D., and Hou, X. (2018). Reversible switch between underwater superaerophilicity and superaerophobicity on the superhydrophobic nanowire-haired mesh for controlling underwater bubble wettability. *AIP Adv.* 8, 045001. <https://doi.org/10.1063/1.5018864>.
- Sheng, X.L., and Zhang, J.H. (2011). Air layer on superhydrophobic surface underwater. *Colloids Surf. A* 377, 374–378. <https://doi.org/10.1016/j.colsurfa.2011.01.033>.
- Shi, C., Cui, X., Xie, L., Liu, Q.X., Chan, D.Y.C., Israelachvili, J.N., and Zeng, H.B. (2015a). Measuring forces and spatiotemporal evolution of thin water films between an air bubble and solid surfaces of different hydrophobicity. *ACS Nano* 9, 95–104. <https://doi.org/10.1021/nn506601j>.
- Shi, C., Cui, X., Zhang, X.R., Tchoukov, P., Liu, Q.X., Encinas, N., Paven, M., Geyer, F., Vollmer, D., Xu, Z.H., et al. (2015b). Interaction between air bubbles and superhydrophobic surfaces in aqueous solutions. *Langmuir* 31, 7317–7327. <https://doi.org/10.1021/acs.langmuir.5b01157>.
- Srinivasan, S., Kleingartner, J.A., Gilbert, J.B., Cohen, R.E., Milne, A.J.B., and McKinley, G.H. (2015). Sustainable drag reduction in turbulent Taylor-Couette flows by depositing sprayable superhydrophobic surfaces. *Phys. Rev. Lett.* 114, 014501. <https://doi.org/10.1103/PhysRevLett.114.014501>.
- Vakarelski, I.U., Chan, D.Y.C., Marston, J.O., and Thoroddsen, S.T. (2013). Dynamic air layer on textured superhydrophobic surfaces. *Langmuir* 29, 11074–11081. <https://doi.org/10.1021/la402306c>.
- Verho, T., Korhonen, J.T., Sainiemi, L., Jokinen, V., Bower, C., Franze, K., Franssila, S., Andrew, P., Ikkala, O., and Ras, R.H.A. (2012). Reversible switching between superhydrophobic states on a hierarchically structured surface. *PNAS* 109, 10210–10213. <https://doi.org/10.1073/pnas.1204328109>.
- Vilaró, I., Yagüe, J.L., and Borrós, S. (2017). Superhydrophobic copper surfaces with anticorrosion properties fabricated by solventless CVD methods. *ACS Appl. Mater. Interfaces* 9, 1057–1065. <https://doi.org/10.1021/acsami.6b12119>.
- Wang, J., Wang, B., and Chen, D. (2014). Underwater drag reduction by gas. *Friction* 2, 295–309. <https://doi.org/10.1007/s40544-014-0070-2>.
- Wang, Y., Yan, W., Frey, M., Vidiella del Blanco, M., Schubert, M., Adobes-Vidal, M., and Cabane, E. (2019). Liquid-like SiO<sub>2</sub>-g-PDMS coatings on wood surfaces with underwater durability, antifouling, antimudgde, and self-healing properties. *Adv. Sustain. Syst.* 3, 1800070. <https://doi.org/10.1002/adusu.201800070>.
- Wu, G.X., Zhao, Y.P., Ge, D.T., Zhao, Y.B., Yang, L.L., and Yang, S. (2021). Highly robust, pressure-resistant superhydrophobic coatings from monolayer assemblies of

chained nanoparticles. *Adv. Mater. Interfaces* **8**, 2000618. <https://doi.org/10.1002/admi.202000681>.

Wu, H.P., Yang, Z., Cao, B.B., Zhang, Z., Zhu, K., Wu, B.B., Jiang, S.F., and Chai, G.Z. (2017). Wetting and dewetting transitions on submerged superhydrophobic surfaces with hierarchical structures. *Langmuir* **33**, 407–416. <https://doi.org/10.1021/acs.langmuir.6b03752>.

Xie, L., Shi, C., Cui, X., and Zeng, H.B. (2017). Surface forces and interaction mechanisms of emulsion drops and gas bubbles in complex fluids. *Langmuir* **33**, 3911–3925. <https://doi.org/10.1021/acs.langmuir.6b04669>.

Yong, J., Chen, F., Huo, J., Fang, Y., Yang, Q., Zhang, J., and Hou, X. (2018). Femtosecond laser

induced underwater superaerophilic and superaerophobic PDMS sheets with through microholes for selective passage of air bubbles and further collection of underwater gas. *Nanoscale* **10**, 3688–3696. <https://doi.org/10.1039/c7nr06920k>.

Yong, J.L., Singh, S.C., Zhan, Z.B., Chen, F., and Guo, C.L. (2019). Substrate-independent, fast, and reversible switching between underwater superaerophobicity and aerophilicity on the femtosecond laser-induced superhydrophobic surfaces for selectively repelling or capturing bubbles in water. *ACS Appl. Mater. Interfaces* **11**, 8667–8675. <https://doi.org/10.1021/acsami.8b21465>.

Zhang, B., Chen, X.M., Dobnikar, J., Wang, Z.K., and Zhang, X.R. (2016). Spontaneous Wenzel

to Cassie dewetting transition on structured surfaces. *Phys. Rev. Fluids* **1**, 073904. <https://doi.org/10.1103/PhysRevFluids.1.073904>.

Zhang, J., Wang, J., Zhang, B., Zeng, Y., Duan, J., and Hou, B. (2020). Fabrication of anodized superhydrophobic 5083 aluminum alloy surface for marine anti-corrosion and anti-biofouling. *J. Oceanol. Limnol.* **38**, 1246–1255. <https://doi.org/10.1007/s00343-020-0036-3>.

Zeiger, C., Kumberg, J., Vullers, F., Worgull, M., Holscher, H., and Kavalenka, M.N. (2017). Selective filtration of oil/water mixtures with bioinspired porous membranes. *RSC Adv.* **7**, 32806–32811. <https://doi.org/10.1039/c7ra05385a>.

## STAR★METHODS

## KEY RESOURCES TABLE

REAGENT or RESOURCE	SOURCE	IDENTIFIER
Chemicals, peptides, and recombinant proteins		
Glass slides	Guluo Glass Co., Ltd.	GL-100100-0.55
L-arginine	Sinopharm Chemical Reagent Co., Ltd.	CAS:74-79-3
Tetraethoxy silane (TEOS)	Sinopharm Chemical Reagent Co., Ltd.	CAS:78-10-4
Ethanol	Sinopharm Chemical Reagent Co., Ltd.	CAS:64-17-5
Isopropanol	Sinopharm Chemical Reagent Co., Ltd.	CAS:67-63-0
HCl	Sinopharm Chemical Reagent Co., Ltd.	CAS: 7647-01-0
NaOH	Sinopharm Chemical Reagent Co., Ltd.	CAS: 1310-73-2
(tridecafluoro-1,1,2,2-tetrahydrooctyl) trichlorosilane (FOTS)	Aladdin Co., Ltd.	>97.0% purity; CAS: 78560-45-9
(heptadecafluoro-1,1,2,2-tetrahydrodecyl) triethoxysilane (HDFTES)	Aladdin Co., Ltd.	96% purity; CAS: 101947-16-4
(3-Aminopropyl) trimethoxysilane (APTMS)	Aladdin Co., Ltd.	97% purity; CAS: 13822-56-5
Software and algorithms		
COMSOL Multiphysics 5.5a	COMSOL	<a href="https://cn.comsol.com/">https://cn.comsol.com/</a>

## RESOURCE AVAILABILITY

## Lead contact

Further information and requests for resources and reagents should be directed to and will be fulfilled by the lead contact, Lili Yang ([liliyang@dhu.edu.cn](mailto:liliyang@dhu.edu.cn)).

## Materials availability

This study did not generate new unique reagents.

## Date and code availability

This study did not generate any unique code or data sets. All data supporting the finding of this study are available within the paper and its [supplemental information](#) files. Any additional information required to reanalyze the data reported in this paper is available from the lead contact upon request. All software's used in this study are commercially available.

## EXPERIMENTAL MODEL AND SUBJECT DETAILS

The experimental samples related to this study are prepared on glass slides (25 mm ×25 mm).

## METHODS DETAILS

## Preparation of recoverable superhydrophobic surfaces

Firstly, chained NPs were synthesized from mixture of L-arginine, silica seeds (~20 nm diameter), deionized (DI) water and tetraethyl orthosilicate with stirring at 60°C for 24 h. Secondly, glass slides were treated with (3-aminopropyl) trimethoxysilane (APTMS) by chemical vapor deposition in a vacuum desiccator for 15 min for the functionalization with amino groups. Excessive APTMS was removed by rinsing the slides with ethanol for 15 s and water for 5 min. Then the treated glass slides were immersed in an aqueous solution of well-dispersed chained NPs (0.05 wt%) at pH=6 for 2 h. After coating, the substrate was rinsed with DI water twice to remove excessive particles. Thirdly, the deposited slides were treated with (tridecafluoro-1,1,2,2-tetrahydrooctyl) trichlorosilane (FOTS) via vapor deposition for 30 min. At last, the slides were heated up to 65°C for 10 min, following by rinsing in acetone and water to remove excess perfluorosilane on surface.

### Fabrication of F-Glass and multi-layered superhydrophobic surfaces

F-Glass means the glass slides after oxygen plasma treatment for 30 min and FOTS treatment via vapor deposition. The preparation method of multi-layered superhydrophobic surfaces could be found in our previous work (Ge et al., 2014). Firstly, chained NPs were reacted with HDFTES and then dispersed in the ethanol solution. Secondly, the solution was loaded into an airbrush with 0.2 mm nozzle size and sprayed repeatedly to obtain multi-layered superhydrophobic surfaces.

### Characterization

The surface morphologies were examined by a field-emission scanning electron microscope (MAIA3, TESCAN, Czech). The static water contact angles were measured from 5- $\mu$ L water droplets by automatic contact angle meter (SL200KB, Kino, USA). The static and dynamic bubble contact angles were recorded from 50- $\mu$ L air bubbles by interface tension meter (OCA40Micro, Dataphysics, Germany). Digital photos and videos were obtained by a digital camera (Nikon 1 J5, Japan). The reflectance monitoring was taken by a USB2000 fiber optical spectrometer (Ocean Optics, USA). The morphology observation was taken by optical microscopy (BX 63, Olympus, Japan).

### Interaction forces between air bubbles and surfaces

The force measurements between air bubbles and solid surfaces in water were conducted using an MFP-3D AFM system (Asylum Research, Santa Barbara, CA) coupled with a Nikon Ti-U inverted microscope. The details of experimental setup were reported previously (Cui et al., 2018; Gong et al., 2019; Shi et al., 2015a). Prior to the force measurements, the glass substrate of the AFM fluid cell was firstly hydrophobized by the octadecyltrichlorosilane (OTS) to possess a water contact angle of  $\sim 60^\circ$  for the immobilization of air bubbles in the following experimental procedure. Air bubbles were generated via a custom-made glass pipet. The air bubble-anchored AFM probe was prepared by using a rectangular AFM tipless cantilever ( $400 \times 70 \times 2 \mu\text{m}^3$ ) with a hydrophobic circular gold patch (diameter  $\sim 65 \mu\text{m}$ , thickness  $\sim 30 \text{nm}$ ) to carefully pick up an air bubble from the hydrophobized glass substrate in water. Then, the bubble probe was moved to the desired solid substrate for surface force measurements. In a typical force measurement, the air bubble-anchored AFM probe was driven by a piezo actuator to approach the solid substrate at a fixed velocity of 1  $\mu\text{m/s}$ , till bubble-surface attachment occurred, and was then retracted for separation. During this process, the deflection of the AFM cantilever was monitored by the laser beam, which was reflected from the backside of the AFM cantilever to a photodiode detector. The spring constant of the cantilever was calibrated using the Hutter and Bechhoefer method (Hutter and Bechhoefer, 1993). In the cases of the ethanol pre-wetting, the solid substrate was firstly wetted using ethanol, followed by immersed in the fluid cell with water immediately. A large amount of water was used to replace the water in the fluid cell to ensure the negligible influence of dissolved ethanol in the force measurements.

### Calculations for the simplifying the sparse surface from chained NPs into truncated nanocone model

To simplify the theoretical analysis of air bubbles growth and stability on our sparse structure, here we simplified our sparse structure into truncated nanocone model. As illustrated in Figure S7, from the AFM profile and through average treatment, the sparse structure from chained NPs could be simplified as truncated nanocone of  $d=150 \text{nm}$ ,  $D=350 \text{nm}$ ,  $H=120 \text{nm}$ ,  $L=1000 \text{nm}$  and  $\alpha=60^\circ$ . Here  $d$ ,  $D$ ,  $H$ ,  $L$  and  $\alpha$  stand for top width, base width, height, distance between truncated nanocones and base angle of truncated nanocone, respectively.

### Calculations for the geometric criteria of truncated nanocone model that allows the air bubble adhere to the top

When the air bubble contacts the top surface of the truncated nanocone structure, as illustrated in Figure S8A, the surface tension between meniscus air/water interface is:

$$F_1 = \gamma \sin \beta \sum s_i \quad (\text{Equation S1})$$

where  $\gamma$  is the surface tension of the gas-liquid interface.  $S_i$  present the contact line length when air bubble contacts the truncated nanocones. Thus, the sum of contact line is:

$$\sum s_i = \pi d' \quad (\text{Equation S2})$$

where  $d'$  is the corresponding section diameter when bubble contacts with truncated nanocone. According to relationship shown in Figure S8C, the angle between surface tension and horizontal direction  $\beta$  is:

$$\beta = \theta - \alpha \quad (\text{Equation S3})$$

where  $\theta$  stands for the intrinsic water contact angle on smooth truncated nanocone surface, which could be considered as water contact angle of F-Glass, thus  $\theta=110^\circ$ . Thus Equation S1 turns into:

$$F_1 = \gamma \pi d' \sin(\theta - \alpha) \quad (\text{Equation S4})$$

### Calculations for the geometric criteria of truncated nanocone model that allows the air bubble fill the closest microstructure

Once adhering to the top surface, the air bubble is expected to repel the water in the cavity beneath and finally fill the whole cavity. According to the Boyle's law, the gas pressure of air bubble is inversely to volume during the vertical spreading:

$$P_0 V_0 = P_1 V_1 \quad (\text{Equation S5})$$

As illustrated in Figure S10, the "0" and "1" states present the air bubble doesn't reach the bottom of microstructure and the air bubble fully fills the cavity, respectively. Thus,

$$V_1 = \pi R_g^2 H \quad (\text{Equation S6})$$

where  $R_g$  represents the geometric diameter of truncated nanocone. Here  $R_g$  varies with the filling depth. then:

$$R_g = \frac{\sqrt{2L - d'}}{2} \quad (\text{Equation S7})$$

where  $d'$  represents the corresponding section diameter when bubble contacts with truncated nanocone. While the volume of air bubble when the filling depth is  $h$  is:

$$V_0 = \pi R_g^2 h + \frac{\pi R_g^3}{3 \cos^3 \theta} (2 - 3 \sin \theta + \sin^3 \theta) \quad (\text{Equation S8})$$

According to the Boyle's law, the gas pressure of air bubble  $P_0$  when the filling depth is  $h$  could be:

$$P_0 = \frac{P_1}{\frac{[2\sqrt{2} - (d+D)/L]}{12 \cos^3 \theta} \frac{1}{H/L} (2 - 3 \sin \theta + \sin^3 \theta) + h/H} \quad (\text{Equation S9})$$

According to the Young-Laplace formula, the relationship between the gas pressure and liquid pressure:

$$P_L - P_0 = -\frac{2 \cos \theta}{R_c} \gamma \quad (\text{Equation S10})$$

where  $R_c$  represents the capillary radius

$$R_c = \frac{2A}{C} \quad (\text{Equation S11})$$

Here  $A$  and  $C$  stand for the horizontal projection area and three-phase contact line length, respectively. There is,

$$A = L^2 - \frac{\pi d'^2}{4} \quad (\text{Equation S12})$$

while the contact line length is:

$$C = \pi d' \quad (\text{Equation S13})$$

Thus,

$$R_c = \frac{4L^2 - \pi d'^2}{2\pi d'} \quad (\text{Equation S14})$$

Here  $d'$  varies with the filling depth. For simplify the calculation here, it is treated approximately as the diameter of truncated nanocone in the middle,

$$d' = \frac{D+d}{2} \quad (\text{Equation S15})$$

Thus, Equation S10 could be transformed into:

$$P_L - \frac{P_1}{\frac{[2\sqrt{2}-(d+D)/L]}{12\cos^3\theta} \frac{1}{H/L} (2-3\sin\theta+\sin^3\theta) + h/H} = -\frac{2\cos\theta}{R_c} \gamma \quad (\text{Equation S16})$$

Then we could finally obtain the equation as:

$$\frac{h}{H} = \frac{P_1}{P_L + \frac{8\pi(D+d)\cos\theta}{16L^2-\pi(D+d)^2}\gamma} - \frac{[2\sqrt{2}-(d+D)/L]}{12\cos^3\theta} \frac{1}{H/L} (2-3\sin\theta+\sin^3\theta) \quad (\text{Equation S17})$$

### Calculations for the geometric criteria of truncated nanocone model that allows the air bubble continue lateral spreading without vertical outgrowth

After the air bubbles expand into the gaps of truncated nanocones, the bubbles are limited by the surface tension  $F_2$  of the meniscus in the vertical direction, as shown in Figure S12. Thus the air bubble pressure  $P_b$  should be smaller than the pressure causing from  $F_2$ , or the air bubble will escape from the surface:

$$P_b < \frac{F_2}{A_2} \quad (\text{Equation S18})$$

where  $A_2$  stands for the vertical projection area of the meniscus. Here the resultant force  $F_2$  could be expressed as:

$$F_2 = \gamma \sin\theta \sum s_i \quad (\text{Equation S19})$$

where  $\sum s_i$  presents the sum arc length of contact line and,

$$\sum s_i = \pi d \quad (\text{Equation S20})$$

The projected area  $A_2$  could be expressed as:

$$A_2 = L^2 \varphi \quad (\text{Equation S21})$$

Thus Equation S18 could be expressed as:

$$P_b < \frac{\gamma \pi d \sin\theta}{L^2 \varphi} \quad (\text{Equation S22})$$

Laterally, the air bubble will contact the convex structure and the bottom surface of the surface, so the bubble will also be limited by the viscous forces from three-phase contact, as shown in  $F_3$  and  $F_4$  in Figure S11. In order to achieve the lateral spreading, the air bubble pressure  $P_b$  should be greater than the pressure from  $(F_3+F_4)$ , thus,

$$P_b > \frac{F_3 + F_4}{A_3} \quad (\text{Equation S23})$$

where  $A_3$  stands for the lateral projection area of the meniscus.

$$F_3 = \gamma S_3 \sin\theta \quad (\text{Equation S24})$$

$$F_4 = \gamma S_4 \cos\theta \quad (\text{Equation S25})$$

where  $S_3$  and  $S_4$  are the corresponding sum length and,

$$S_3 = \frac{2H}{\sin\alpha} \quad (\text{Equation S26})$$

$$S_4 = L \quad (\text{Equation S27})$$

Here the lateral projection area of the meniscus:

$$A_3 = HL \quad (\text{Equation S28})$$

Thus Equation S23 could be expressed as:

$$P_b < \frac{\gamma(2H \sin\theta + L \cos\theta \sin\alpha)}{HL \sin\alpha} \quad (\text{Equation S29})$$

According to the Equations S22 and S29, then

$$\frac{\gamma(2H \sin \theta + L \cos \theta \sin \alpha)}{HL \sin \alpha} < \frac{\gamma \pi d \sin \theta}{L^2 \varphi} \quad (\text{Equation S30})$$

which could be transformed as:

$$H/L < \frac{-\cos \theta \sin \alpha}{2 \sin \theta (1 - \sin \alpha \sqrt{\pi(1 - \varphi)}/\varphi)} \quad (\text{Equation S31})$$

During the continuous repelling in the cavity of air bubble, the meniscus should not reach the bottom of microstructure, as illustrated in Figure S13. Thus the height of truncated nanocone  $H$  should be greater than the maximum depth of meniscus:

$$H > h \quad (\text{Equation S32})$$

According to Figure S13B,

$$h = (\sqrt{2}L - d) \frac{1 - \sin \varepsilon}{2 \cos \varepsilon} \quad (\text{Equation S33})$$

where  $\varepsilon$  is the angle between the curvature radius of meniscus and horizontal direction. It has a relationship with the advancing angle of water on the truncated nanocone surface,

$$\varepsilon = 270^\circ - \alpha - \theta_{adv} \quad (\text{Equation S34})$$

Then Equation S33 turns into:

$$h = (\sqrt{2}L - d) \frac{1 - \sin(270^\circ - \alpha - \theta_{adv})}{2 \cos(270^\circ - \alpha - \theta_{adv})} \quad (\text{Equation S35})$$

From Equation S32, it could be deduced:

$$H/L > (\sqrt{2} - 2\sqrt{(1 - \varphi)/\pi}) \frac{1 - \sin(270^\circ - \alpha - \theta_{adv})}{2 \cos(270^\circ - \alpha - \theta_{adv})} \quad (\text{Equation S36})$$

Combining Equations S31 and S36, the geometric criterion of  $H/L$  could be given by:

$$\left( \sqrt{2} - 2\sqrt{(1 - \varphi)/\pi} \right) \frac{1 - \sin(270^\circ - \alpha - \theta_{adv})}{2 \cos(270^\circ - \alpha - \theta_{adv})} < H/L < \frac{-\cos \theta \sin \alpha}{2 \sin \theta (1 - \sin \alpha \sqrt{\pi(1 - \varphi)}/\varphi)} \quad (\text{Equation S37})$$

### Calculations of spreading radius of air bubble on truncated nanocone microstructured surface

The spreading radius of air bubble on truncated nanocone microstructured surface is calculated by the spreading radius ratio with the spreading radius of air bubble on smooth fluorinated surface (F-Glass). As illustrated in Figure S17, we assume that the viscous forces from the surface tension during the spreading on microstructured surface  $F_r$  or smooth surface  $F_f$  is equal. Thus:

$$F_r = F_f \quad (\text{Equation S38})$$

For the smooth fluorinated surface, the viscous force has a relationship with the intrinsic water contact angle  $\theta$ :

$$F_f = -\gamma 2\pi R_0 \cos \theta \quad (\text{Equation S39})$$

As illustrated in Figure S18, during the air bubble spreading, the liquid-air-solid contact line extends along the sides, bottom surfaces and top surfaces of truncated nanocones. First, the bubble extends up along the truncated nanocone and around the bottom of the truncated nanocone. An elliptical gas-liquid-solid contact line begins to form. Secondly, the bubble moves around the bottom to the other side of the truncated nanocone and a complete elliptical gas-liquid-solid contact line on the surface of the truncated nanocone forms. Then, the bubble extends upward along the truncated nanocone, and the elliptical gas-liquid-solid contact line moves along the direction of the bubble until the left side of the gas-liquid-solid interface contact line reaches the highest point of the truncated nanocone. Fourthly, the elliptical three-phase contact line moves upward and gets shorter gradually and then bubble contacts with the top surface of the truncated nanocone and moves along the direction of the bubble spreading until it is completely separated from the top surface of the truncated nanocone. Here these three parts of viscous forces are set as  $F_a$ ,

$F_b$  and  $F_c$ .  $a$ ,  $b$  and  $c$  represent the three-phase contact line length when bubble spreads along the sides, bottom surfaces and top surfaces, respectively. Thus,

$$F_r = N(F_a + F_b + F_c) \quad (\text{Equation S40})$$

Here  $N$  is the number of truncated nanocones which contact with air bubble when spreading. And,  $N$  has relationship with the spreading radius  $R$ :

$$N = \frac{2\pi R}{L} \quad (\text{Equation S41})$$

According to the analysis of  $F_a$  when the bubble moves around the truncated nanocone side, as illustrated in [Figure S19](#), the surface tension of three-phase contact line in the first stage is advance force for the spreading of air bubble. While the  $F_a$  offsets each other when the air bubble in the second stage. Therefore, it is believed that the greatest viscous force for the spreading of air bubble appears when the air bubble move to the middle of top surface truncated nanocone.

In order to predict the viscous force  $F_a$  when the air bubble moves to the middle of top surface, as illustrated in [Figure S21](#),  $v$ ,  $a_1$  and  $a_2$  stand for the air bubble movement speed, the water height difference between two sides of truncated nanocone and the movement distance of air bubble along the bottom of truncated nanocone. Let's assume that the movement speed along all directions is the same. Here  $F_a$  could be expressed as:

$$F_a = F_x \int_0^\pi k \sin \beta d\beta = \gamma \sin \theta \int_0^\pi k \sin \beta d\beta \quad (\text{Equation S42})$$

where  $F_x$ ,  $k$  and  $\beta$  stand for the viscous force of any point on the ellipse, distance between the point in the ellipse and the center of ellipse, and the angle between  $F_x$ . In order to simplify the integral calculation, it is assumed that the ellipse line on the truncated nanocone model is equivalent to the ellipse line on the post model with diameter of  $d$ . Thus,

$$F_a \approx 2l_3 \gamma \sin \theta \quad (\text{Equation S43})$$

here  $l_3$  is the major semiaxes of ellipse lengths. [Equation S43](#) will be transformed into if  $l_3 = \frac{d}{2}$ :

$$F_a \approx \gamma d \sin \theta \quad (\text{Equation S44})$$

According to the schematic in [Figure S22](#), the viscous force from the three-phase interface along the bottom could be calculated as:

$$F_b = -\gamma b \cos \theta \quad (\text{Equation S45})$$

while  $b$  is the three-phase contact line length when contacting with the bottom. During the spreading of air bubble, length  $b$  varies. And,

$$b_{\max} = L \quad (\text{Equation S46})$$

Thus,

$$F_b \leq -\gamma L \cos \theta \quad (\text{Equation S47})$$

As illustrated in [Figure S23](#), the viscous force along the top surface of truncated nanocone during the air bubble spreading  $F_c$  reaches the maximum when the line is in the middle of top surface, Thus, the maximum of  $F_c$  is:

$$F_c \leq -\gamma d \cos \theta \quad (\text{Equation S48})$$

According to [Equations S40](#), [S41](#), [S44](#), [S47](#), and [S48](#), then the maximum viscous forces during air bubble lateral spreading,

$$F_r = 2\gamma\pi R \frac{d \cdot \sin \theta}{L} - 2\gamma\pi R \cos \theta - \frac{2\gamma\pi R \cos \theta d}{L} \quad (\text{Equation S49})$$

Then [Equation S38](#) could be expressed as:

$$-\gamma 2\pi R_1 \cos \theta = 2\gamma\pi R \frac{d \cdot \sin \theta}{L} - 2\gamma\pi R \cos \theta - \frac{2\gamma\pi R \cos \theta d}{L} \quad (\text{Equation S50})$$

If  $D=5d$ , then Equation S50 could be transformed into:

$$\frac{R}{R_0} = \frac{-\cos \theta}{\frac{D}{L} \frac{\sin \theta}{5} - \cos \theta - \frac{D}{L} \frac{\cos \theta}{5}} \quad (\text{Equation S51})$$

### Dynamic simulation

The numerical simulations of dynamic bubble spreading in submarine was based on laminar flow model via COMSOL Multiphysics 5.5a. There are three assumptions: (i) the wall temperature is constant, and no heat transfer occurs at the gas-liquid interface, (ii) the two phases composed of bubbles and liquid film on the wall were incompressible Newtonian fluids, and (iii) the numerical calculation was for the two-dimensional flow situation and the flow process was laminar flow. The Gas-liquid two-phase distribution was calculated by the solid two-phase flow and level set (transient) physics field. The water contact angle on the wetted solid surface was  $72^\circ$ . The remaining boundaries were non-slip walls. Under the gravitational field, the result of bubbles floating up and interacting with the micro-nano structure within 0.01 s was calculated and analyzed based on the built-in transient Navier-Stokes equations.

### QUANTIFICATION AND STATISTICAL ANALYSIS

The statistical results of contact angles were from 3 different samples.